Transonic Computational Method for an Aft-Mounted Nacelle/Pylon with Power Effect

L. T. Chen*, K. C. Yu†, and T. Q. Dang‡
Douglas Aircraft Company, Long Beach, California 90846

A computational method has been developed for computing transonic flows about an aft-fuselage mounted capped-nacelle/pylon configuration with/without propeller power. A hybrid conformal-mapping/transfinite-interpolation scheme is developed to generate body conforming grid systems; a multigrid line-relaxation scheme is applied to solve the potential flowfield; an Euler correction method based on the Clebsch transformation is employed to simulate the power effect; and an inverse boundary-layer method is incorporated to calculate the viscous flows over the pylon and fuselage surfaces. Included are comparisons of the solutions with available test data and the solutions of a panel method. The importance of the fuselage boundary-layer effect on the pylon pressure distribution is studied. The present method has been shown to be reliable, efficient, and general and has been successfully applied to compute a wide range of flow conditions, including those of high angles of attack.

I. Introduction

THE advanced turboprop design of the next-generation transport aircraft has been of great interest to many airline companies in the past several years. However, because of the geometric complexity of the configuration, the optimal integration of the turboprop engine, nacelle, pylon, and fuselage to minimize interference drag and to increase the buffet boundary has become a great challenge to aerodynamic designers. A reliable and efficient transonic computational method is required to reduce the amount of expensive and time-consuming wind tunnel tests. In this paper, a transonic computational method is described for calculating flows over an aft-fuselage mounted nacelle/pylon configuration with or without propeller power effects. A capped nacelle without modeling of the inlet flow is considered.

The transonic full-potential/boundary-layer method[1] developed earlier for computing flowfields about a general wing/body configuration has been adapted and extended for the present configuration. The grid generation method of Ref. 1 was modified and incorporated with a transfinite grid generation method to generate a grid system about an aft-fuselage mounted nacelle/pylon configuration. A multigrid relaxation method was developed to solve the full potential equation; the inverse boundary-layer method of Cebeci et al.[2] was applied to compute the viscous effect; and an Euler correction method using the Clebsch transformation[3] was developed to simulate propeller power effect.

II. Grid Generation Method

The aft-fuselage mounted nacelle/pylon configuration of interest is shown in Fig. 1. A grid topology that provides a natural clustering of mesh lines near the nacelle nose and pylon leading edge is employed. The grid system is designed to resolve high pressure gradients near nacelle nose and pylon leading edge and thus allows the method to compute cases with very high angles of attack. It is also designed to simulate the power effect so that the mesh lines on nacelle cross-sectional surfaces form near circles such that they can easily be made to conform to the actuator disk.

The grid system is generated in inboard and outboard regions separately, as shown in Fig. 2. The two-block grid system is generated in several steps. The grid system in each block is generated as an extension of an earlier wing/body grid generation method,[1] and the grid on the dividing plane of the two blocks are matched point by point. A vertical plane dividing the nacelle surface in halves is first defined, and a series of C-mesh lines, which conform to the nacelle contour in the vertical plane, are generated. The inboard region extends from the fuselage surface to the nacelle vertical plane and covers the aft-fuselage, pylon and the inboard half of the nacelle surfaces, whereas the outboard region extends from the outboard half of the nacelle surface to the spanwise farfield. With the C-mesh lines defined in the vertical plane, the spanwise cross sections defined on the pylon surface and the fictitious plane extending from the outboard nacelle to the spanwise farfield, a series of shell surfaces approximately conforming to the nacelle surface are formed. A conformal mapping procedure was developed to generate C-meshes on each shell surface.

An additional procedure, applying a transfinite interpolation scheme, was developed to conform the mesh lines to both the nacelle and fuselage surfaces. Interpolation in the transfinite method is performed by a set of blending functions such as Lagrangian interpolation polynomials and splines while maintaining precise control of mesh size and orthogonality conditions near the surface boundaries. More details of the grid generation method are described in Ref. 4.

A global view of a nacelle/pylon/fuselage grid system is presented in Fig. 3. The surface grid distributions, the actuator disk, half of the symmetry plane, half of the spanwise farfield boundary, and the downstream farfield boundary planes are shown. Both the fuselage and nacelle surfaces are modeled by a system of body-conforming C-mesh lines, and the pylon surface is modeled by another system of C-mesh lines, which cluster naturally near the pylon leading edge. Figure 4 shows a horizontal cross plane touching the pylon leading-edge line and the upper surface of the pylon. The line extending from the nacelle nose point is curved toward the symmetry plane and ends at the symmetry plane. This grid topology is designed to facilitate the implementation of the

Presented as Paper 89-0560 at the AIAA 27th Aerospace Sciences Meeting, Reno, Nevada, Jan. 9–12, 1989; received July 16, 1989; revision received Jan. 5, 1990; accepted for publication May 22, 1990.

*Aerodynamics Technology, Senior Staff Engineer. Member AIAA.
†Aerodynamic Systems and Processes, Senior Engineer/Scientist. Member AIAA.
‡Currently Assistant Professor, Dept. of Mechanical and Aerospace Engineering, Syracuse University, Syracuse, NY.

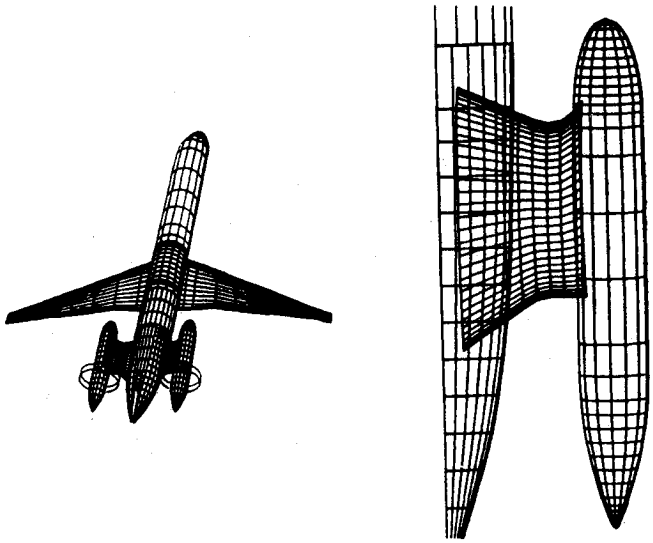

Fig. 1 A typical aft-fuselage mounted nacelle/pylon configuration.

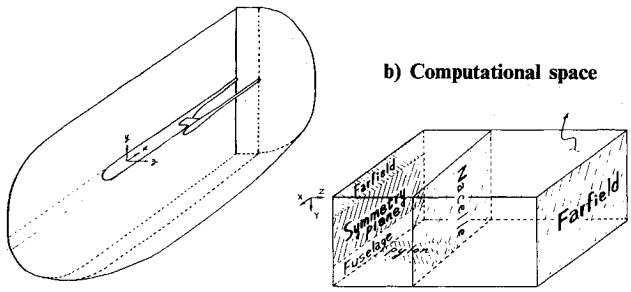

Fig. 2 Two-block grid system.

multigrid scheme. During the multigrid cycles, corrections are computed in a sequence of meshes. A sequence of coarser meshes is generated by continuously eliminating every other point in each direction. The nacelle nose point and the most upstream point on the symmetry plane, positioned along the same mesh line, always remain as points in the coarse meshes such that the upstream farfield location and the nacelle nose point are not altered during the multigrid cycle. This ensures a successful multigrid scheme. Figure 5 shows a constant-I cross-sectional surface near the pylon midchord. The mesh lines are conformed to the fuselage surface, symmetry plane, and nacelle surface through the application of the transfinite interpolation scheme.

III. Full-Potential Method

To solve the potential flowfield, the finite volume method of Jameson and Caughey[5] and the fully and partially conservative and nonconservative schemes of Chen[6] are used.

The full potential equation to be solved is given by

$$(a^2-u^2)\phi_{xx}+(a^2-v^2)\phi_{yy}+(a^2-w^2)\phi_{zz} - 2uv\phi_{xy}-2vw\phi_{yz}-2uw\phi_{xz}=0 \quad (1)$$

Here ϕ is the total-potential function; u, v, w are the x, y, z components of the flow velocity, respectively; and a is the local speed of sound determined from the energy equation

$$a^2=a_0^2-[(\gamma-1)/2]q^2 \quad (2)$$

where γ is the ratio of specific heats for the assumed calorically perfect gas, q the total velocity, and a_0 the stagnation speed of sound.

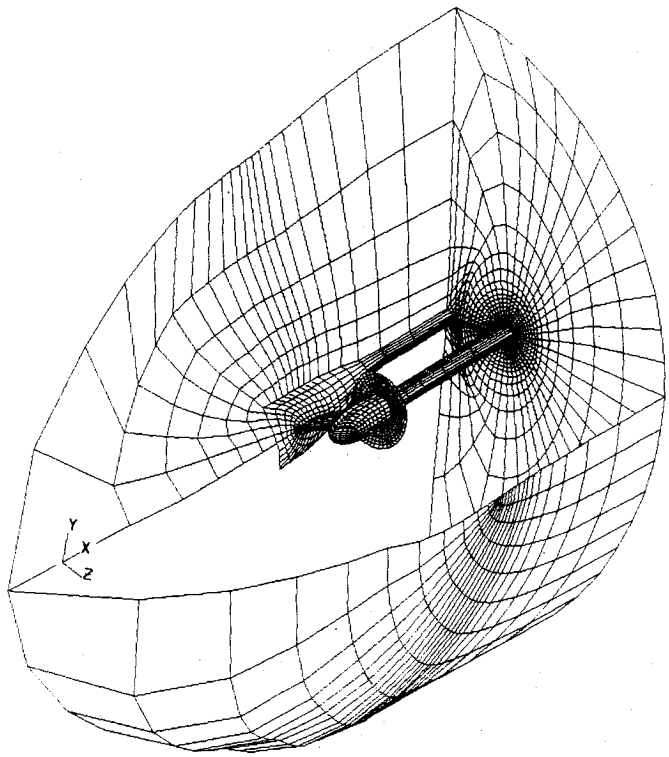

Fig. 3 A global view of a grid system about a demo nacelle/pylon/fuselage configuration.

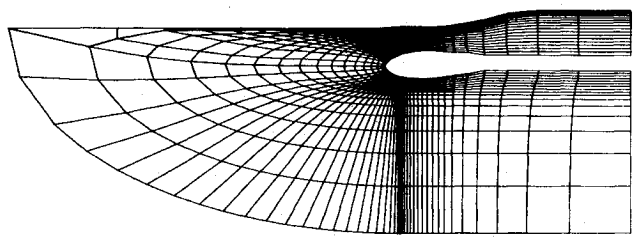

Fig. 4 Grid distribution on a horizontal plane.

In conservation form, the full-potential equation can be written in the computational coordinates (X,Y,Z) as

$$(\rho hU)_X+(\rho hV)_Y+(\rho hW)_Z=0 \quad (3)$$

where

$$\rho=\{1+[(\gamma-1)/2]M_\infty^2(\phi_x^2+\phi_y^2+\phi_z^2)\}^{1/(\gamma-1)} \quad (4)$$

and M_∞ is the freestream Mach number. The h denotes the determinant of the Jacobian matrix H of the transformation, and U, V and W are the contravariant components of the velocity vector.

In order to reflect the type-dependent nature of the transonic full potential equation, the artificial viscosities, as suggested by Chen,[6] are added to its finite-difference approximation.

The second derivative of the potential function in the streamwise direction s is given as

$$d_{SS}=1/q^2(U^2\phi_{XX}+V^2\phi_{YY}+W^2\phi_{ZZ} +2UV\phi_{XY}+2VW\phi_{YZ}+2UW\phi_{XZ}) \quad (5)$$

The directional bias of supersonic flows can be properly simulated by performing an unwind differencing or adding artificial viscosities in the approximate streamwise direction.

If Y = constant lines are in the approximate s direction, the principal part of ϕ_{SS} is approximated by

$$\phi_{SS} \simeq (U^2/q^2)\phi_{XX} + (V^2/q^2)\phi_{YY} \tag{6}$$

The details of the scheme are described in Ref. 5.

The artificial viscosity terms are normally added when the local Mach number exceeds the critical Mach number Q_c of 1. Slightly smaller values of Q_c between 0.9 and 1.0 may result in slightly stronger shocks and may possibly remove undesirable aft-shock re-expansion in the calculations. A study of the effect of Q_c value is given later.

In order to facilitate the implementation of the multigrid scheme, the two-block grid systems are rearranged to form a single-block grid system. The relaxation sweep direction affects the stability of the scheme. A relaxation sweep in the direction strongly against the flow direction in the supersonic region normally leads to divergent solutions. A K-plane sweep starts from the fuselage symmetry plane and the spanwise farfield and marches toward the nacelle surface from both inboard and outboard directions. This sweep scheme ensures that the sweep direction is not aganist the flow direction upstream of the nacelle. On each K plane, two relaxation schemes applying sweeps in the X and Y direction, respectively, were developed. The scheme applying alternating X- and Y-direction sweeps converges best; however, if there is a significantly large supersonic region near the nacelle nose, the Y-direction sweep fails to converge and only the X-direction sweep leads to converged solutions.

The freestream condition is imposed in the upstream and the spanwise farfields. Since the reduced potential function is solved, the freestream condition simply implies that the reduced potential function is zero on the farfield boundary. At the downstream infinity, the velocity component in the x direction is set to be the freestream value. The boundary conditions in all the farfields are of Dirichlet type which generally gives a better overall convergence rate than the Neumann-type farfield boundary condition.

IV. Simulation of Propeller Power Effect

The rotational flowfield downstream of the propeller can be described by the Euler equations. Various methods have been developed to solve the Euler equations. The present method is based on the decomposition of the velocity vector into irrotational and rotational parts. The irrotational part is obtained by solving a modified full-potential equation, whereas the rotational part is obtained by solving two convective-type equations governing the convection of enthalpy. The multigrid line-relaxation scheme described earlier is applied to solve the modified full-potential equation. An Euler correction method developed earlier by Dang and Chen[3] based on the Clebsch transformation is applied here for solving the flowfield downstream of the propeller modeled by an actuator disk. In the present study, only counter-rotating propellers are considered so that there is no swirl in the flow downstream of the propeller. Other transonic methods based on the actuator disk theory were developed to simulate propeller power effect by solving the Euler equations.[7] The Euler methods based on the time-marching scheme are generally computationally more expensive than the present method.

Based on the Clebsch transformation and the assumption that the velocity vector can be decomposed into a potential and a rotational part, one can write

$$V = \nabla\phi + (h_0 - h_\infty)\nabla t \tag{7}$$

where h_0 and h_∞ are the total enthalpy of the flow and the freestream, respectively. The governing equations for the potential function ϕ and two Clebsch variables h_0 and t can be expressed as

$$\nabla \cdot (\rho\nabla\phi) = -\nabla \cdot [\rho_0(h - h_\infty)\nabla t] \tag{8}$$

$$V \cdot \nabla h_0 = 0 \tag{9}$$

$$V \cdot \nabla t = 1 \tag{10}$$

with the speed of sound a given by

$$a^2 = (\gamma - 1)(h_0 - h_\infty) + \{1/M_\infty^2 + [(\gamma - 1)/2](1 - q^2)\} \tag{11}$$

and the density ρ given by

$$\rho = \left[\left(\frac{h_0}{h_\infty}\right)\frac{1 + (\gamma + 1)/2M_\infty^2}{1 + (\gamma - 1)/2M^2}\right]^{1/(\gamma - 1)} \tag{12}$$

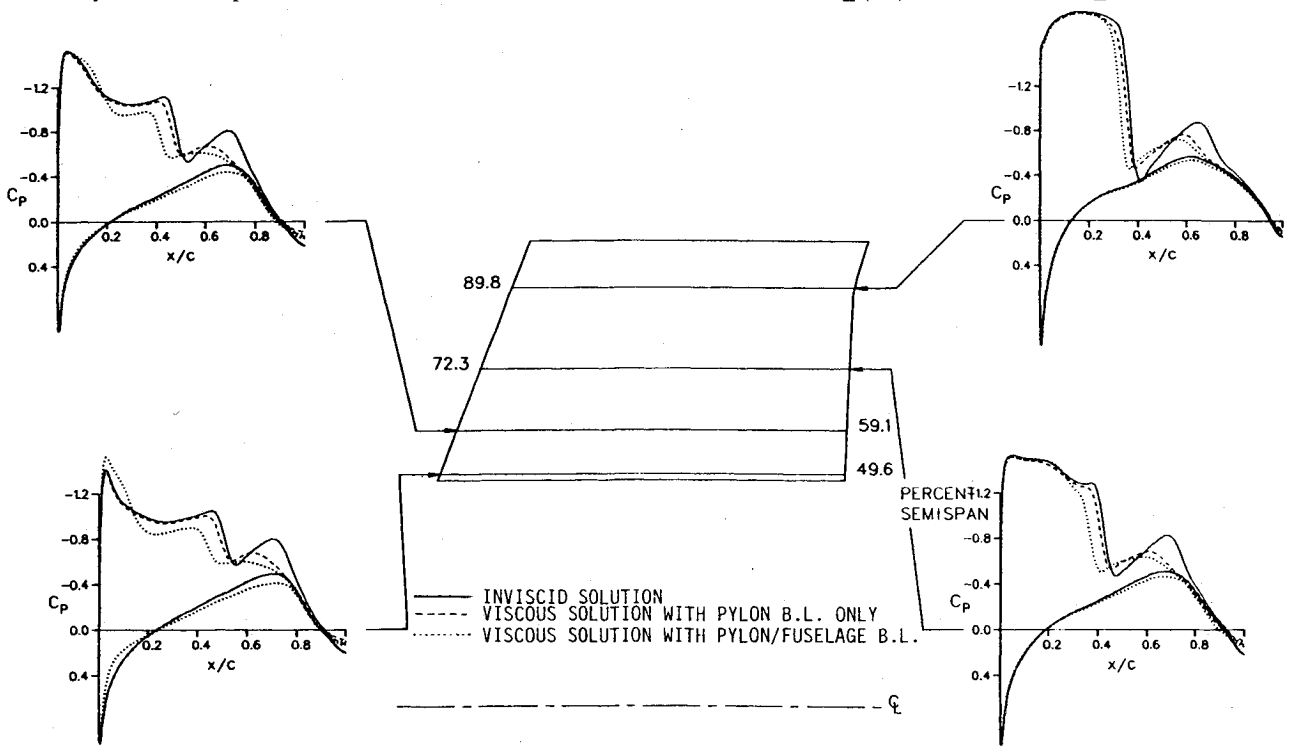

Fig. 5 Comparison of inviscid and interactive viscous solutions obtained for configuration A at $M_\infty = 0.76$ and $\alpha = 5$ deg.

In the transformed coordinates (X,Y,Z), U, V and W are now defined as

$$\begin{vmatrix} U \\ V \\ W \end{vmatrix} = (H^T H)^{-1} \begin{vmatrix} \phi_X + (h_0 - h_\infty)t_X \\ \phi_Y + (h_0 - h_\infty)t_Y \\ \phi_Z + (h_0 - h_\infty)t_Z \end{vmatrix} \tag{13}$$

whereas Eqs. (9) and (10) can be rewritten as

$$U\frac{\partial h_0}{\partial X} + V\frac{\partial h_0}{\partial Y} + W\frac{\partial h_0}{\partial Z} = 0 \tag{14}$$

$$U\frac{\partial t}{\partial X} + V\frac{\partial t}{\partial Y} + W\frac{\partial t}{\partial Z} = 1 \tag{15}$$

The transformed equations of the Clebsch variables h_0 and t can be solved numerically as described in Ref. 3. In the present method, h_0 and t are solved analytically based on small perturbation approximations, as described in the following. The stagnation enthalpy h_0 is assumed to be convected along the mesh lines, i.e.,

$$\frac{\partial h_0}{\partial X} = 0 \tag{16}$$

and the drift time t is assumed to be convected by a characteristic speed u^* such that

$$\frac{\partial t}{\partial x} = \frac{1}{u^*} = \text{const} \tag{17}$$

where u^* is taken to be the flow speed just downstream of the actuator disk and can be approximated as

$$u^* = \frac{1}{2}\left(1 + \sqrt{1 + \frac{T}{(1/2)A_d \rho_\infty u_\infty^2}}\right) \tag{18}$$

where T is the thrust and A_d the actuator disk area. With a prescribed total-enthalpy-jump distribution on the actuator disk and the use of Eqs. (16) and (18), the modified full-potential equation, Eq. (8), can be solved.

A study was made to solve Eqs. (14) and (15) numerically[8] without using the small perturbation approximation. The results show that the pressure distributions obtained on the pylon surface with and without the small perturbation approximation are nearly the same.

V. Viscous/Inviscid Interaction Scheme

The inverse boundary-layer method developed by Cebeci et al.[2] for coupling with the transonic full-potential method is applied in the present method on the pylon surface in the strip theory sense to account for the pylon viscous effect, whereas an axisymmetric boundary-layer method based on the Mangler transformation[9] is applied on the fuselage surface to account for the fuselage viscous effect.

The boundary-layer method computes the displacement thickness using the inviscid surface velocity distribution as the edge velocity just outside the boundary layer. Two approaches can be used for coupling the inviscid and viscous flow solutions. In the displacement approach, the displacement thickness is added to the inviscid geometry in the normal direction; the near-field grid distribution is then redistributed to accommodate the new geometry. In the blowing approach, the wing geometry and the grid system remain unchanged, whereas the no-flux surface boundary condition applied in the inviscid-flow calculation is modified to allow a prescribed surface blowing condition, accounting for the addition or subtraction of mass flux through the surface to maintain the growth or decay of displacement thickness along the streamwise direction.

The blowing approach has been shown to be more reliable in treating cases with large displacement thickness than the displacement approach. The details of the implementation of both approaches are described in Ref. 2. In the present study, the blowing approach is adopted on both the pylon and fuselage surfaces.

The pylon boundary-layer calculation in the present method is similar to the wing boundary-layer calculation.[3] Since the mesh lines on the pylon surfaces are nearly aligned with streamlines, the two-dimensional strip theory can be applied along mesh lines on the surface. The interactive procedure developed for the wing boundary-layer calculation in Ref. 2 is applied here for the pylon boundary-layer calculation.

The fuselage boundary-layer effect in the present aft-fuselage configuration is more important than in the wing/fuselage configuration simply because the fuselage boundary layer develops over a longer distance from the fuselage nose in the present configuration. As the fuselage boundary layer develops, its thickness grows rapidly near the aft-end of the fuselage because of the sudden reduction of the fuselage cross-sectional area, causing significant modifications to the fuselage upsweep and also to the passage cross-section area between the fuselage and the nacelle. The nacelle boundary-layer thickness on the nacelle surface is much thinner than that of the fuselage surface, therefore the effect of nacelle boundary layer is not included in the present study.

In the present method, the fuselage surface is represented by a series of C-mesh lines. The approximate streamlines are prescribed first on the fuselage surface. A surface interpolation scheme is employed to interpolate flow solutions between the C-mesh lines and the approximate streamlines on the fuselage surface. The axisymmetric boundary-layer method[9] is then applied to calculate the viscous flow along each approximate streamline with a prescribed radius distribution. The initial boundary-layer velocity profiles are defined at a prescribed distance from the fuselage nose. The computed displacement thickness distributions along approximate streamlines are then used to compute the blowing velocity distributions along the C-mesh lines through the surface interpolation scheme. The fuselage surface boundary condition with nonzero-blowing velocity distributions is then imposed in the inviscid flow calculation.

VI. Interactive Viscous/Inviscid Solutions

The interactive viscous/inviscid solutions obtained for a Douglas wind-tunnel nacelle/pylon fuselage, configuration A, are presented in this section. The boundary-layer calculations were performed for every four to six invisid flow calculations. For most calculations, 80 work units were sufficient to get a converged solution and required about 180 s of CRAY-XMP CPU time. If not stated otherwise, the nonconservative scheme was used in the inviscid flow calculations, and the critical Mach number Q_c was set to be 1. If the fuselage boundary-layer calculation was performed, the fuselage nose was set to be 11 pylon-root-chord lengths upstream of the pylon leading edge and the initial fuselage boundary-layer velocity profile was computed according to the location of the fuselage nose. For all calculations, a total number of $161 \times 23 \times 33$ grid points are used.

Comparisons of the inviscid and the interactive viscous solutions obtained for configuration A at $M_\infty = 0.76$, $Re = 2.79 \times 10^6$, based on the pylon-root-chord length and $\alpha = 5$ deg are presented in Fig. 5. Three sets of solutions are shown. These are the inviscid solution, the viscous solution obtained with the pylon boundary-layer calculation only, and the viscous solution obtained with both the pylon and fuselage boundary-layer calculations. The fuselage boundary-layer effect is obvious in this case. As shown in Fig. 5, the inviscid solution has a distinct double-shock pattern on the upper surface. By adding the pylon viscous effect, the strength of the

second shock is reduced and its location is moved upstream by about 5–10% chord length, but there is only slight modification of the prediction of the first shock. The fuselage boundary-layer effect, on the other hand, modifies both the first and second shocks dramatically. The first shock is moved upstream by about 10% of the chord over the entire span, and its strength is also reduced significantly, whereas the second shock almost disappears. The suction peak near the pylon root is sharply increased due to a sudden growth of the fuselage boundary layer near the pylon leading edge. Because the shocks formed near the nacelle are stronger than the shocks formed near the fuselage, the flow near the nacelle separates at the shock root and remains separated for about 5–8% chord length before it reattaches at the after-shock re-expansion followed by further separation near the trailing edge.

The present solutions computed at 50 and 92% semispan stations are compared with the test data at two flow conditions as shown in Figs. 6 and 7. Figure 6 presents the computed pressure distribution on the pylon surface at $M_\infty = 0.760$ and $\alpha = 1.2$ deg. Two solutions were obtained with the pylon viscous effect only, and one with both the pylon and the fuselage viscous effects, respectively. The fuselage viscous effect moves the shock about 3% chord upstream and significantly reduces the pressure level downstream of the shock and improves the agreement between the computed solutions and test data. Figure 7 presents a comparison of two computed solutions with test data at $M_\infty = 0.800$ and $\alpha = -4$ deg. Two solutions were obtained with the pylon boundary-layer effect only and the pylon/fuselage boundary-layer effects, respectively. The fuselage viscous effect is again very pronounced in this case. The computed solution with the pylon/fuselage boundary-layer effects agrees much better with the test data.

A study of the effect of the critical Mach number Q_c is presented in Fig. 8. Two solutions were obtained at $M_\infty = 0.8$ and $\alpha = 2$ deg with $Q_c = 1.00$ and 0.95, respectively. The solution obtained with $Q_c = 1.00$ shows a strong flow re-expansion downstream of the upper-surface shocks over the entire span. This re-expansion nearly disappears in the solution obtained with $Q_c = 0.95$. The shock computed with $Q_c = 0.95$ is also slightly more downstream than the shock computed with $Q_c = 1.00$. The flow re-expansion downstream of strong shock is normally not evident in experimental results. In the present case, the solution obtained with $Q_c = 0.95$ agrees with test data better than the one with $Q_c = 1.0$.

VII. Numerical Results with Propeller Power

The power simulation method described in Sec. IV was applied to two configurations. The solutions obtained at subsonic speed are compared with the solutions of the panel method and test data. The solutions at transonic speed are presented to study the power effect on the shock calculations. The present study assumes that the flowfield behind the actuator disk is isentropic and has no jump in either the radial or the tangential velocities. At high thrust loading coefficients such as the takeoff/climbing conditions, the small perturbation approximations in the present method are probably not adquate for predicting flowfields downstream of the propeller. However, this is not crucial since for these particular configu-

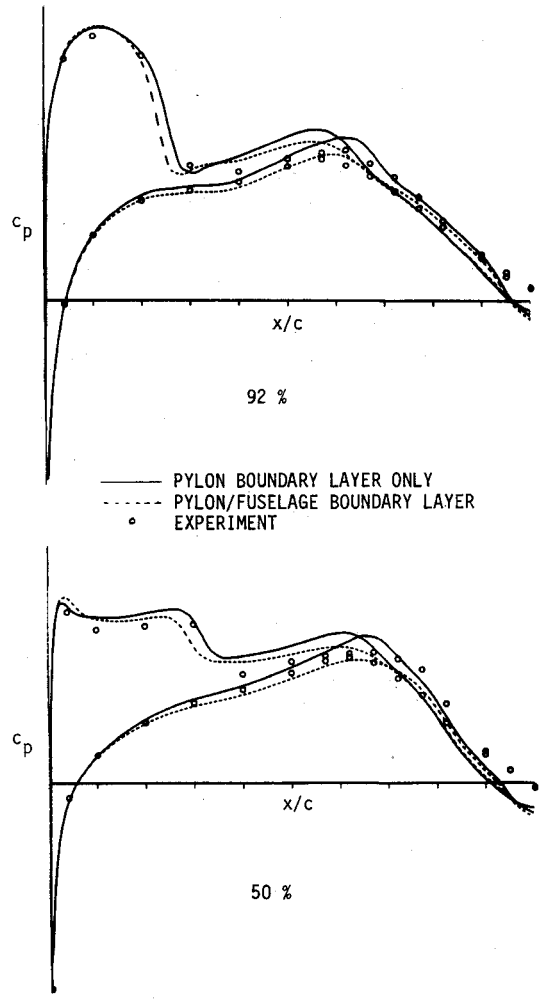

Fig. 6 Comparison of present solutions with test data for the nacelle/pylon/fuselage configuration at $M_\infty = 0.760$ and $\alpha = 1.2$ deg.

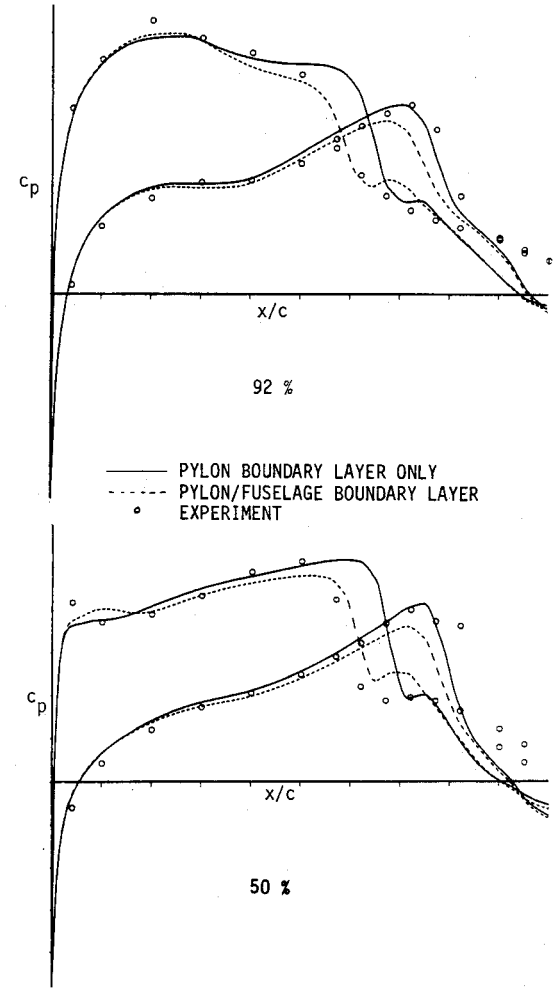

Fig. 7 Comparison of present solutions with test data for the configuration A at $M_\infty = 0.8$ and $\alpha = -4$ deg.

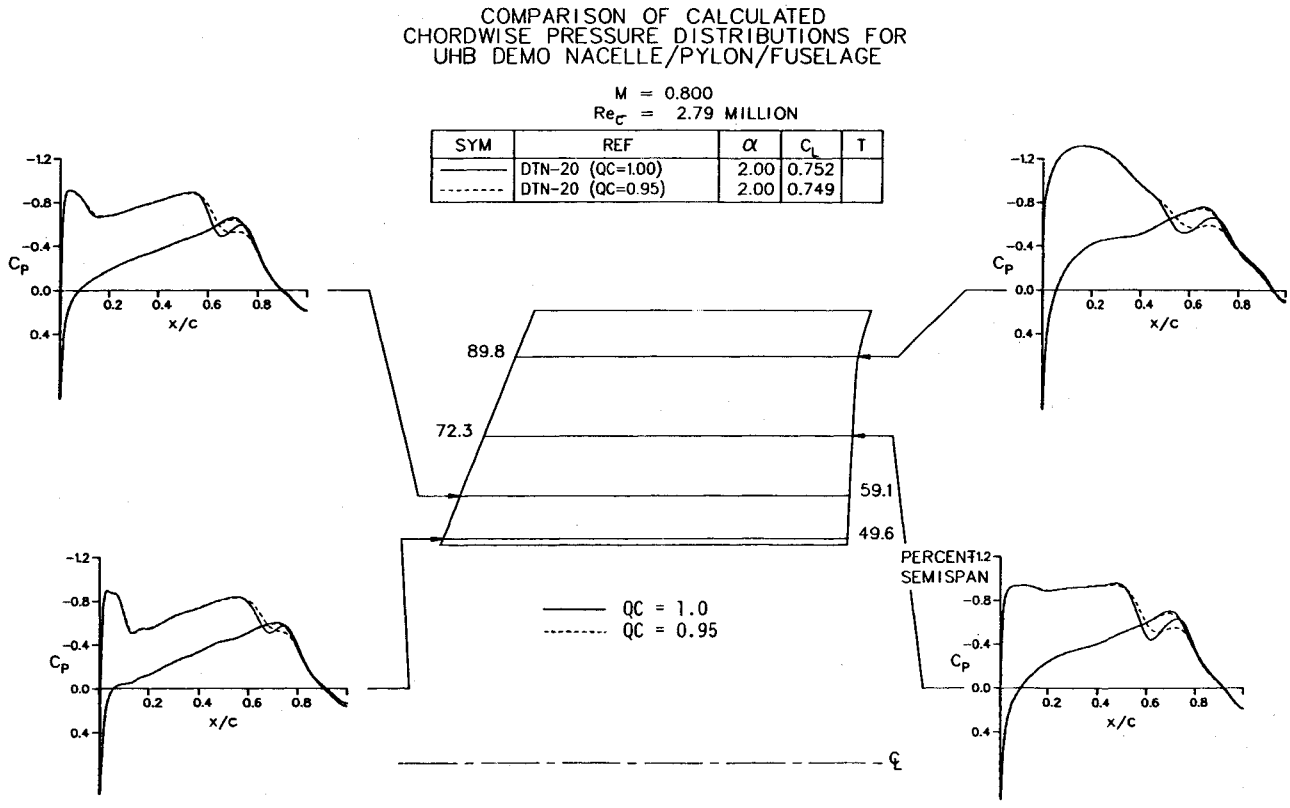

Fig. 8 A study of the effect of critical Mach number Q_c.

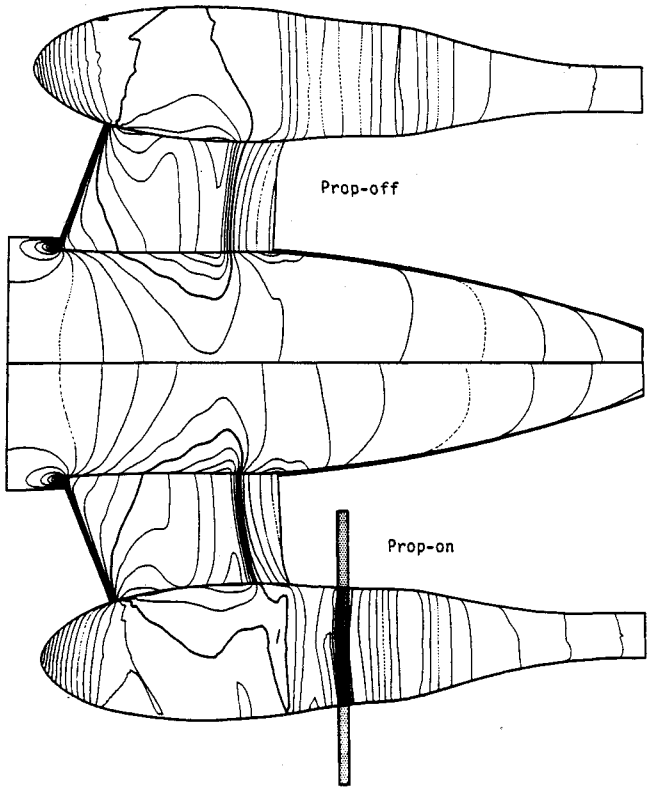

Fig. 9 Comparison of isobar solutions for demo nacelle/pylon/fuselage with and without power at $M_\infty = 0.800$, $\alpha = 1$ deg, and $T/QA_d = 0.24$.

rations, the main region of interest to the designers is on the pylon and the fuselage, which do not lie within the rotational flow region. Our earlier studies[8] indicate that the pylon solutions were mainly affected by the amount of suction of the actuator disk theory.

Figure 9 illustrates a comparison of the solutions with prop off and prop on for configuration A near the buffet condition at $M_\infty = 0.80$ and $\alpha = -1$ deg. In the prop-on case, a thrust loading coefficient of 0.24 was used, which was roughly equal to the thrust required to balance the predicted drag at this flight condition. This figure shows that in the transonic flow regime the effect of power is confined to a small region near the propeller. When shocks appear on the pylon near the trailing edge, as in the present case, the effect of power is to increase the shock strength and move the shocks further downstream.

The power-off and -on test data for a Douglas test mode, configuration B, are compared with the calculations in Figs. 10 and 11. The agreements are very good, especially the predicted pressure increments due to power. Also shown for comparison are the solutions of the panel method.[10,11] The overall agreement between these two computational methods is good although the panel method and the present method model the bound/shed vorticity structure very differently. These comparisons indicate that the loading characteristics of the propeller blade appear to be unimportant for this application. The interference effect is mainly characterized by the suction caused by the propeller and/or the amount of the propeller slipstream contraction, which is a strong function of the thrust loading coefficient.

The interactive viscous/inviscid solutions obtained with both pylon and fuselage boundary-layer calculations and with/without power effect are presented in Figs. 12 and 13 for configuration A. There are no experimental or flight data available for comparison. Figure 12 presents a comparison of the solutions obtained at $M_\infty = 0.80$, $\alpha = 2.0$, and $Re = 2.79 \times 10^6$ with and without power effect. The power-on solution was obtained at $T/QA_d = 0.24$. Under the effect of the propeller power, the shock near the pylon root on the upper surface moves about 7% chord downstream, and near the nacelle, where the power effect is most prominent, the shock moves about 15% chord downstream. The pressure peaks on the lower surface also increase significantly with power on. A comparison of the computed separation con-

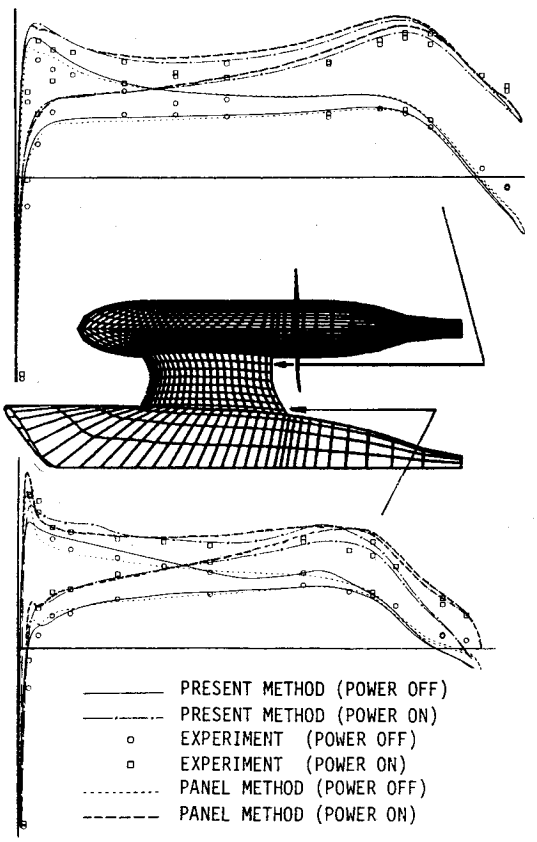

Fig. 10 Comparison of computed pylon pressure distributions and test data for configuration B with and without power at $M_\infty = 0.2$, $\alpha = -3$ deg, and $T/QA_d = 0.2$.

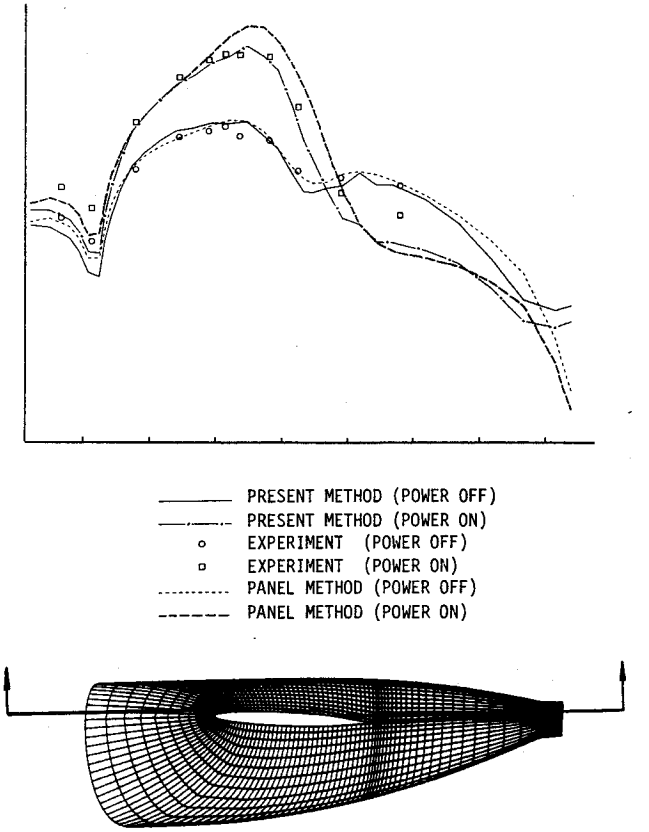

Fig. 11 Comparison of computed fuselage pressure distributions and test data for configuration B with and without power at $M_\infty = 0.2$, $\alpha = -3$ deg, and $T/QA_d = 0.2$.

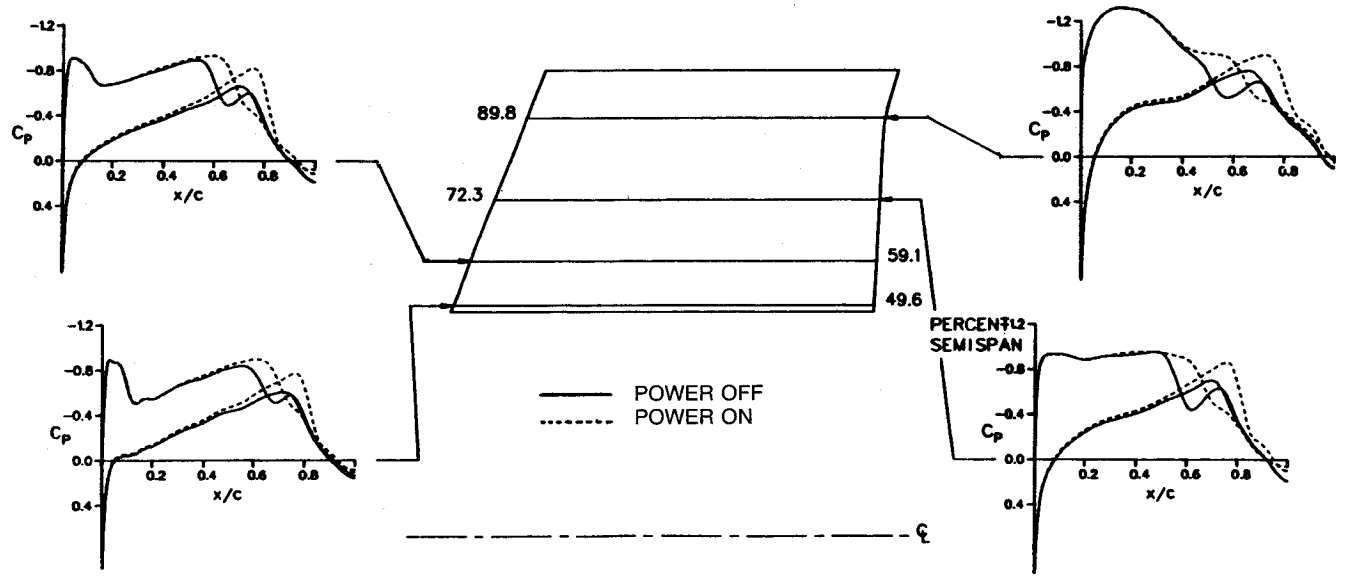

Fig. 12 Comparison of the computed pressure distributions for power-off and power-on cases for configuration A at $M_\infty = 0.800$, $\alpha = -2$ deg, and $T/QA_d = 0.24$.

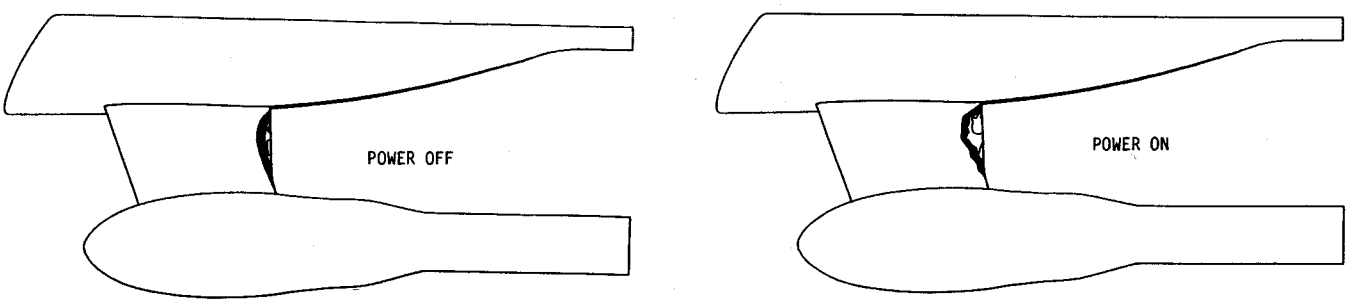

Fig. 13 Comparison of the computed separation contours for power-off and power-on cases.

tours with and without power is presented in Fig. 13. The flow separation region increases significantly in the chordwise direction under the propeller power effect.

VIII. Conclusion

An efficient and reliable transonic computational method has been developed for computing transonic flowfields about a general aft-fuselage mounted capped-nacelle/pylon configuration with propeller power effect. The grid topology of the present method is designed for flowfield calculations over a wide range of angle of attack and also for modeling of the actuator disk.

A series of comparison of the solutions with test data were made for several wind-tunnel test configurations. The inverse boundary-layer method was applied on both the pylon and fuselage surfaces. The effect of the fuselage boundary layer was found to be significant on the pylon solutions in the transonic regime. The fuselage boundary layer modified the fuselage upsweep and the passage cross-sectional area between the fuselage and nacelle and, as a result, modified the computed shocks.

The Euler correction method, based on a Clebsch transformation, has been successfully developed and applied to study the propeller power effects in both subsonic and transonic speed regimes.

References

[1]Chen, L. T., Vassberg, J. C., and Peavey, C. C., "A Transonic Wing-Body Flowfield Calculation with Improved Grid Topology," *AIAA Journal*, Vol. 23, Dec. 1985, pp. 1877–1884.

[2]Cebeci, T., Chen, L. T., and Chang, K. C., "An Interactive Scheme for Three-Dimensional Transonic Flows," *Numerical and Physical Aspects of Aerodynamic Flows III*, edited by T. Cebeci, Springer-Verlag, New York, 1986, pp. 412–431.

[3]Dang, T. Q., and Chen, L. T., "Euler Correction Method for Two- and Three-Dimensional Transonic Flows," *AIAA Journal*, Vol. 27, Oct. 1989, pp. 1377–1386.

[4]Yu, K. C., and Chen, L. T., "A Grid Generation Method for an Aft-Fuselage Mounted Capped-Nacelle/Pylon Configuration with an Actuator Disk," AIAA Paper 90-1564, June 1990.

[5]Jameson, A., and Caughey, D. A., "A Finite-Volume Method for Transonic Potential Flow Calculation," *Proceedings of AIAA 3rd Computational Fluid Dynamics Conference*, AIAA, New York, June 1977, pp. 35–54.

[6]Chen, L. T., "A More Accurate Transonic Computational Method for Wing-Body Configuration," *AIAA Journal*, Vol. 21, June 1983, pp. 848–855.

[7]Yu, N. J., and Chen, H. C., "Flow Simulations for Nacelle Propeller Configurations Using Euler Equations," AIAA Paper 84-2143, 1984.

[8]Dang, T. Q., "Simulations of Propeller/Airframe Interference Effects Using an Euler-Clebsch Method," *Journal of Aircraft*, Vol. 26, No. 11, Nov. 1989, pp. 994–1001.

[9]Cebeci, T., "Laminar and Turbulent Incompressible Boundary Layers on Slender Bodies of Revolution in Axial Flow," *Journal of Basic Engineering*, Vol. 29, 1970, p. 545.

[10]Hess, J. L., Friedman, D. M., and Clark, R. W., "Calculation of Compressible Flow About Three-Dimensional Inlets with Auxiliary Inlets, Slats and Vanes by Means of a Panel Method," NASA CR-174975, June 1985.

[11]Valarezo, W. O., and Hess, J. L., "Time-Averaged Subsonic Propeller Flowfield Calculations," AIAA Paper 86-1807, June 1986.